

Observation of Grain Boundary Sliding in a Lamellar Ultrafine-Grained Steel

Laura Ahmels, Sebastian Bruns, Karsten Durst, and Enrico Bruder*

The deformation behavior of a ferrite steel with ultrafine-grained (UFG) lamellar microstructure generated by linear flow splitting is investigated and compared to a coarser cold-worked reference state, using a set of complementary local deformation and microstructural characterizations methods. The pile-up around indentations shows a pronounced anisotropy for the UFG lamellar microstructure indicating the relative motion of grains along their elongated boundaries. This observation is confirmed by stepwise compression testing of micropillars along the normal direction of lamellar-shaped grains using a new faceted pillar geometry to image the initial microstructure and its evolution throughout the test. The surface roughening in pillar compression testing can be categorized into the formation of discrete steps at the surface along particular grain boundaries and a more gradual roughening that is attributed to intragranular dislocation slip. Potential mechanisms for the observed grain boundary sliding are discussed taking several factors such as the strain rate sensitivity and potential Coble creep rates into account. In conclusion, a grain boundary sliding process carried by grain boundary dislocations appears to be the most likely explanation for the observed behavior.

boundaries not only act as obstacles for lattice dislocation motion, but also enable deformation mechanisms that do not play a significant role in coarse-grained materials.^[5,6] The transition of deformation mechanisms at large plastic strains is also related to the strain saturation stage that has been unveiled by SPD processing, which marks the point where strain hardening vanishes and the length scales of the microstructure remain constant and its morphology self-similar.^[7] The dominant deformation mechanisms and the role of grain boundary-mediated processes in SPD-deformed materials have been investigated extensively.^[1,6,8–12] Yet, a generalized theory is still lacking and may not even be appropriate, considering that a variety of deformation mechanisms have been reported to occur in UFG and NC materials, depending on the material and processing conditions, such as shear band formation, grain boundary migration, or grain boundary sliding.

1. Introduction


The development of severe plastic deformation (SPD) methods over the last decades has opened up a new field of metal plasticity, allowing the formation of bulk ultrafine-grained (UFG) and nanocrystalline (NC) metals at low homologous temperatures. These materials exhibit a range of unique properties and a plastic behavior differing from conventional coarse-grained materials.^[1–4] This is caused by their high defect density, in particular the increased amount of grain boundaries. These grain

The formation of nonadiabatic shear bands has been reported to be pronounced in UFG materials due to the limited or even nonexistent strain hardening capacity, especially in bcc metals that also exhibit a reduced strain rate sensitivity in the UFG or NC regime.^[13] In iron with grain sizes between 80 and 300 nm produced by powder consolidation, nearly all plastic deformation has been found to be carried by shear bands.^[14,15] While some authors suggest that the shear bands in UFG and NC materials are formed by grain rotation processes,^[5] others suggest that cooperative grain boundary sliding processes are involved.^[10,16]

The migration of grain boundaries in UFG metals during plastic deformation has been observed via quasi in situ electron backscatter diffraction (EBSD) measurements on high-pressure torsion (HPT)-processed copper subjected to subsequent cold rolling.^[17] The authors conclude that this mechanism controls the formation of a steady-state regime (i.e., a regime in which the grain size does not change during further straining) in cold rolling. Similarly, grain boundary migration is also suggested to be responsible for the formation of the steady state during HPT.^[7]

The occurrence of grain boundary sliding, that is, a translation of grains against each other along their shared grain boundary in rigid body-type motion, is another deformation mechanism that is often considered to be relevant for the plastic behavior of UFG metals. While in coarse-grained materials it only occurs at

L. Ahmels, S. Bruns, K. Durst, E. Bruder
Physical Metallurgy (PhM)
Materials Science Department
Technical University of Darmstadt
Peter-Grünberg-Straße 2, 64287 Darmstadt, Germany
E-mail: e.bruder@phm.tu-darmstadt.de

 The ORCID identification number(s) for the author(s) of this article can be found under <https://doi.org/10.1002/adem.202400267>.

© 2024 The Author(s). Advanced Engineering Materials published by Wiley-VCH GmbH. This is an open access article under the terms of the Creative Commons Attribution-NonCommercial-NoDerivs License, which permits use and distribution in any medium, provided the original work is properly cited, the use is non-commercial and no modifications or adaptations are made.

DOI: 10.1002/adem.202400267

elevated temperatures,^[18] it has been observed at ambient temperature in several UFG materials that were processed by SPD.^[8,10,16] Generally, two underlying mechanisms are discussed; diffusion along grain boundaries (Coble creep) or motion of grain boundary dislocations.^[19] Some authors restrict the term “grain boundary sliding” to the diffusion-controlled deformation process, whereas in this work, the term is used as a phenomenological description. Even though there are several models for the yield strength prediction of NC and UFG materials taking into account diffusion based grain boundary sliding,^[20,21] experimental investigations often do not allow a direct identification of the underlying mechanism that is causing the sliding process. Grain boundary sliding is experimentally observed in the form of steps along grain boundaries at the sample surface around a Vickers indent in equal channel angular pressing (ECAP)-processed aluminum^[8] as well as at the surface of tensile specimen from ECAP-processed nickel and copper.^[16] Similarly, Ivanov et al.^[22] attributed the deformation relief evolving on polished tensile specimen from ECAP-processed aluminum to be caused by a mixture of grain boundary sliding, shear bands, and intragranular dislocation slip. In contrast, the deformation of FIB grid on the cross section of a nickel HPT sample does not show any signs of grain boundary sliding during further HPT processing.^[23]

A variety of direct and indirect methods has been used to investigate the governing deformation mechanisms in UFG and NC materials, with both categories having certain limitations or deficiencies. In case of in situ transmission electron microscopy (TEM) observations, the high amount of free surface raises doubts about whether the results reflect the bulk behavior of the material. Similarly, in case of in-situ straining or postmortem investigations of bulk specimen only surfaces can be observed, whereas the microstructure within the specimen and its evolution during straining remain unknown. Tomographic methods that could potentially overcome this limitation are currently still lacking the resolution to precisely capture the grain shape and spatial arrangement of UFG or NC microstructures.

Another approach is to investigate lamellar microstructures with only one dimension in the UFG/NC regime. Due to the low thickness of the grains in 1D, grain boundary-mediated deformation processes might occur, while the higher grain size in the other 2D allows the production of specimen with an approximately constant microstructure perpendicular to the observation direction.

Such a lamellar microstructure can be produced by severe cold rolling, or the linear flow splitting (LFS) process, which is known for reaching a steady state of grain refinement.^[24–26] In this incremental forming process, the band edge of a sheet metal is formed into a y-shaped profile (process details can be found in refs. [24,27,28]). Close to the split surface of a LFS profile, high compressive strains cause the formation of a strongly elongated UFG microstructure with rolling-type texture. The thickness of the elongated grains perpendicular to the flange surface lies in the order of 100 nm while the grain dimensions in the other two directions can range up to a few micrometers. This microstructure is constant parallel to the split surface but exhibits a strong gradient in the perpendicular direction with grain sizes increasing with increasing distance to the split surface. Near the lower flange surface, a conventional cold rolled

microstructure is found. Once a steady state has been reached, the gradient microstructure stays constant when submitted to further splitting steps, suggesting that at least near the split surface plastic deformation has to occur without being accompanied by further grain refinement.

Due to the strongly elongated microstructure as well as the pronounced microstructural gradient perpendicular to the flange surface, LFS profiles do not only offer the possibility to investigate the deformation mechanisms occurring in UFG materials, but also facilitate a direct comparison to coarser microstructures that were subjected to lower plastic strains by choosing a higher distance to the split surface.

The aim of this work therefore is to investigate the deformation mechanisms in the lamellar UFG microstructure of LFS profiles. To determine whether the UFG microstructure shows a different bulk deformation behavior compared to a conventional cold worked microstructure, the strain rate sensitivity of both microstructures is measured using nanoindentation and the resulting surface deformation structures around the indents are compared. To identify the deformation mechanisms in the UFG region, micropillars are produced by focused ion beam (FIB) milling and incrementally compressed inside an scanning electron microscopy (SEM) while imaging the microstructure before, in between, and after the compression increments. To ensure the relevance of these micromechanical experiments the results are compared to the deformation behavior observed in the indentation experiments.

2. Experimental Section

LFS profile made from a 2 mm-thick HC480LA-grade steel sheet with the following chemical composition 0.07 wt% C, 0.71 wt% Mn, 0.1 wt% Cr, 0.047 wt% Si, 0.034 wt% Nb, and 0.016 wt% Al was used for all investigations. The material exhibited a ferritic microstructure with spherical Fe₃C precipitates of up to 1 μm diameter. LFS was conducted in 20 steps with an incremental splitting depth of 1 mm, leading to a flange span of 26 mm, as schematically shown in **Figure 1**. For further details on the LFS process and resulting characteristic UFG gradient microstructures, we refer to earlier works.^[24–31] For microstructural analysis, a sample of the profile was ground and polished down to 0.25 μm diamond suspension, and the final polishing step was performed using OPS suspension for 5 min. The microstructure in distances of 30 and 600 μm to the split surface was characterized by performing EBSD analyses on a cross section (rolling direction–normal direction [RD–ND] plane, see **Figure 1**). The measurements were carried out using a MIRA3-XMH SEM (TESCAN) equipped with a DigiView V EBSD system (EDAX). The parameters were chosen according to the local microstructure, the measurement in a distance of 30 μm was carried out on an area of 700 μm² using an acceleration voltage of 15 kV and a step size of 20 nm. The measurement in 600 μm distance to the split surface was performed on an area of 1700 μm² with an acceleration voltage of 20 kV and a step size of 30 nm. All EBSD measurements were analyzed using the TSL OIM Analysis software (EDAX). The cleanup routines Grain CI Standardization and Grain Dilation (single iteration) were performed on all datasets.

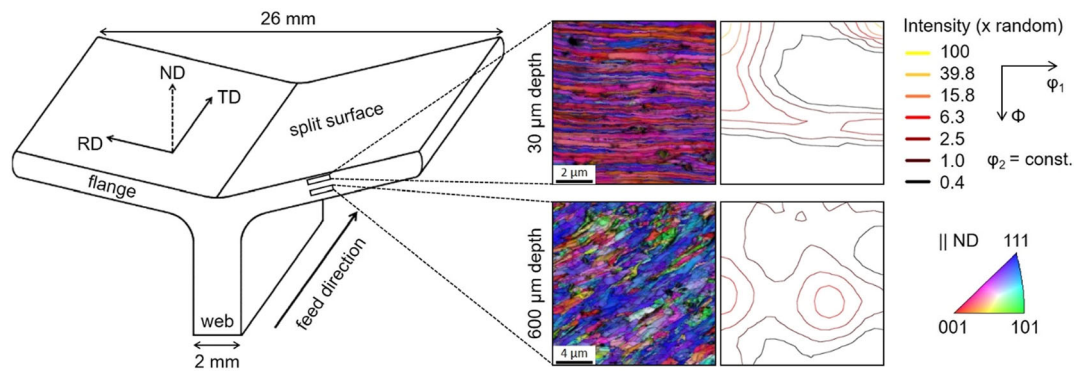


Figure 1. Schematic of the linear flow split profile geometry (left) and corresponding inverse pole figure maps and orientation distribution functions at $\varphi_2 = 45^\circ$ (right) acquired at 30 and 600 μm distance to the split surface.

Only points with a confidence index exceeding 0.1 were considered in the evaluation.

To characterize the deformation behavior of the LFS microstructure, hardness indents were performed on the cross section in distances of 30 and 600 μm to the split surface using a G200 nanoindenter (KLA) with a cone tip exhibiting an opening angle of 60° and a spherical top part with a radius of 5 μm . The tests were carried out in continuous stiffness measurement mode using indentation strain rates of $\dot{\epsilon} = \frac{\dot{p}}{P} = 10^{-1}, 10^{-2}$, and 10^{-3} s^{-1} (where P is the indentation load) to a target maximum indentation depth of 2 μm . For both distances to the split surface seven indentations with a spacing of 60 μm were done at each of the three strain rates. The hardness values determined by the indents were averaged and used to determine the strain rate sensitivity $m = \frac{\partial \ln(H)}{\partial \ln(\dot{\epsilon})}$.

The deformation behavior of the material surrounding the indents was characterized by SE imaging using an acceleration voltage of 15 kV. In addition, the samples were repolished using 0.25 μm diamond suspension and the polishing agent Masterprep (Buehler) before carrying out EBSD measurements on an indent with a strain rate $\dot{\epsilon} = 10^{-3} \text{ s}^{-1}$ for both distances to the split surface. For each depth, the parameters were chosen to be the same as in the previous microstructural investigation.

For the pillar compression experiments, the split surface as well as one of the RD–ND edges was carefully ground and polished, removing a layer of $\approx 30 \mu\text{m}$ from the split surface which was determined measuring the size reduction of a hardness indent before and after preparation. Eight micropillars with a diameter of 5 μm and a height of 8–10 μm were milled into the sample surfaces at the polished edge using a Zeiss Auriga 60 Focus Ion Beam (FIB) at the Karlsruhe Nano Micro Facility. A facet was cut into the pillars and additional material in their vicinity was removed to allow EBSD analyses and back-scattered electron (BSE) imaging. A schematic drawing and SEM image of the pillar geometry is shown in the Appendix (Figure A1). For reference tests, cylindrical pillars without facet with 5 μm diameter and 10 μm height as well as 10 μm diameter and 15 μm height were also prepared (five each).

The initial microstructure of the pillars was imaged using BSE as well as EBSD with an acceleration voltage of 15 kV

and a step size of 10 nm. The pillars were then stepwise compressed inside an SEM using an InSEM nanoindenter (KLA) with a flat punch tip (Synton-MDP). In each increment, a displacement of 300 nm was aimed at using a constant displacement rate of 10 nm s^{-1} . In between the deformation steps, the changes in the microstructure of the pillars were documented by BSE imaging up to the point where surface roughening prevented further imaging based on channeling contrast. The cylindrical reference pillars were tested with a strain rate jump (SRJ) method that was varying the displacement rate between 10 and 1 nm s^{-1} .

The facet of some of the less severely deformed pillars was subsequently repolished to allow EBSD measurements after deformation. In an additional step, 200 nm of the facet were removed by FIB milling and the pillars were imaged again using EBSD to gain information about the microstructure perpendicular to the pillar facet.

3. Results

The microstructure in 30 μm distance to the split surface shown in Figure 1 exhibits a strongly elongated “pancake” UFG microstructure with rolling-type texture that is characteristic of the region close to the split surface of LFS-processed material.^[29,30] In 600 μm distance to the split surface, a coarser microstructure with weaker texture containing a lot of subgrain structures is found. The difference in texture is most pronounced in the α -fiber area fraction that decreases from 72% close to the split surface to 30% in 600 μm distance. The inverse grain boundary density as a measure of the grain size increases from $S_v^{-1} = 0.11 \mu\text{m}$ to $S_v^{-1} = 0.41 \mu\text{m}$ within the same distance. Additionally, the elongation direction of the microstructure changes. While the long axis of the grains near the split surface lies parallel to the split surface, it shows an angle of roughly 45° to it in 600 μm distance. For a higher-resolution microstructural investigation based on TEM crystal orientation mapping of the elongated UFG microstructure, we refer to an earlier publication.^[31]

The differences in microstructure are also reflected in the hardness values found in 30 and 600 μm distance to the split surface. For all strain rates and in accordance to previous

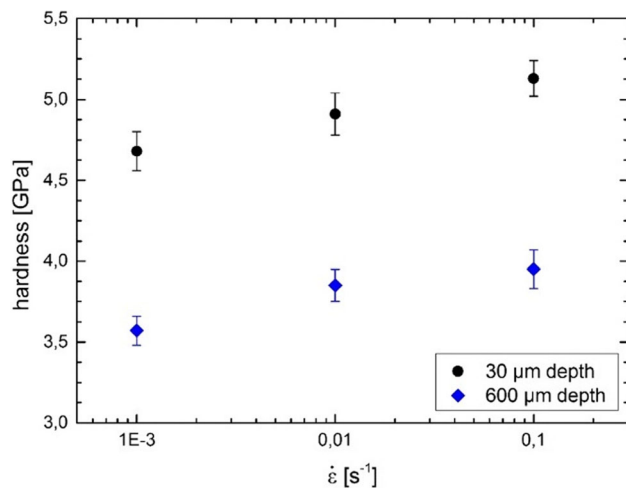


Figure 2. Hardness as a function of indentation strain rate at a distance of 30 and 600 μm to the split surface.

investigations,^[29,32] the hardness decreases with increasing distance to the split surface as shown in **Figure 2**. For a strain rate of $\dot{\epsilon} = 10^{-2} \text{ s}^{-1}$, a hardness of 4.9 GPa is found in 30 μm distance to the split surface as compared to 3.9 GPa at a distance of 600 μm. The corresponding strain rate sensitivities are $m = 0.019$ at 30 μm to the split surface and $m = 0.022$ in a depth of

600 μm, that is, there are only very minor differences in strain rate sensitivity between the different depths. These values are much lower than the value reported for fully annealed iron of $m = 0.054$ ^[33] but in a similar range as the strain rate sensitivities found in SPD-processed iron and ferrite steel.^[9,33]

To examine the plastic flow during nanoindentation, the deformation zones around the indents on the sample surface are investigated via SEM using SE imaging to visualize the topography as well as EBSD after repolishing to remove the pile-up and related surface roughening. At 600 μm to the split surface, the pile-up of the material in the plastic zone surrounding the indent shows only a slightly preferred orientation parallel to the grain elongation direction, that is, in 45° to the vertical axis, whereas a lot of features are oriented in radial direction of the indent (**Figure 3a**). In contrast, the pile-up at 30 μm to the split surface is very anisotropic, showing a much wider spacing perpendicular to the direction of grain elongation than parallel to it as indicated by white lines in **Figure 3d**. The UFG pancake microstructure also affects the pile-up topography. Some distinct surface steps parallel to the elongation direction are apparent, indicating a relative motion of lamellar grains parallel to each other. A comparison of the indents performed with different strain rates is shown in the Appendix (**Figure A2**) and reveals no qualitative change of the pile-up behavior with changing strain rate.

In the inverse pole figure (IPF) and local orientation spread maps from EBSD, the area with increased orientation deviation

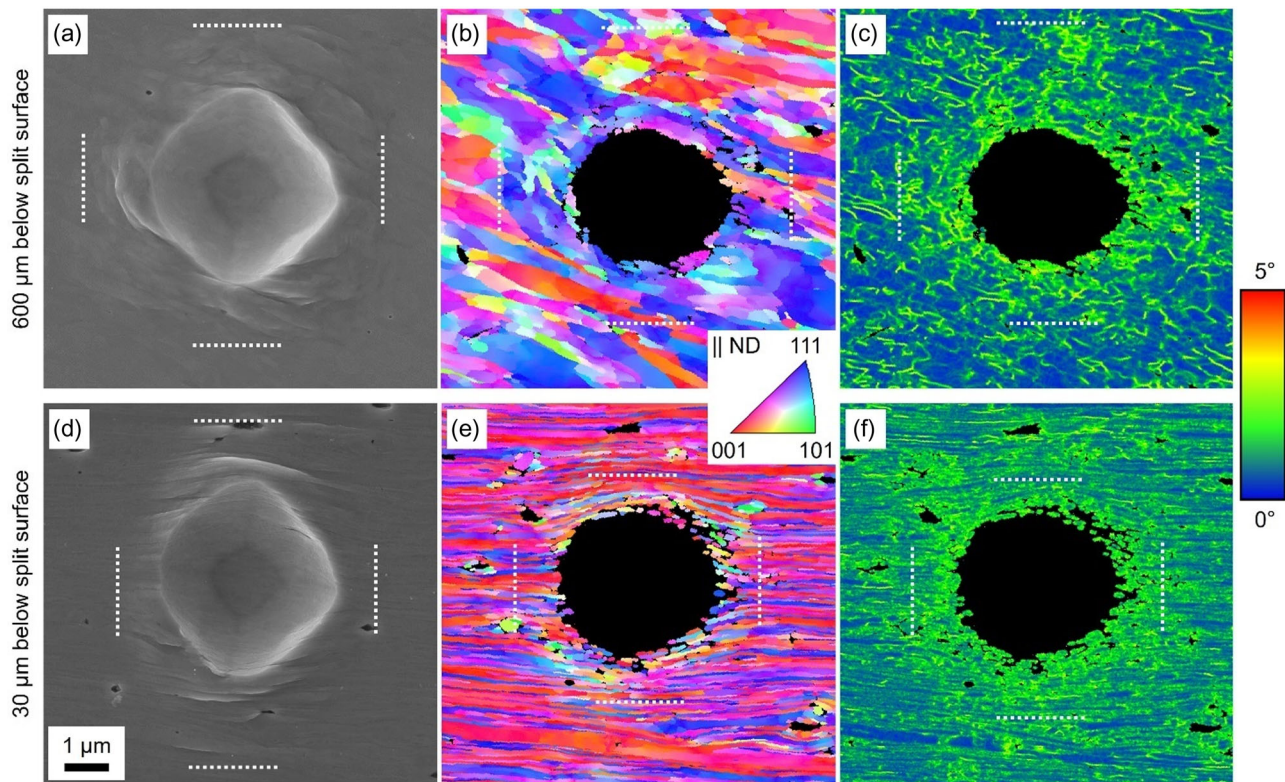


Figure 3. a,d) SE image, b,e) IPF map, c,f) and local orientation spread map in the vicinity of indents in a–c) 600 μm and in d–f) 30 μm distance to the split surface performed with an indentation strain rate of 10^{-3} s^{-1} . White lines indicate the extension of the indentation-induced plastic zone.

within grains, that is, increased grain substructures, is marked. This area indicates the zone in which a considerable amount of dislocation-based plasticity occurred during indentation. At $600\ \mu\text{m}$ to the split surface, the area marked in the SE image is of a similar size compared to the one marked in the EBSD maps. The comparable dimension of the pile-up region and the area of increased grain orientation spread indicates that the plastic deformation induced by the indent is predominately carried by dislocation activity for the cold worked microstructure. At $30\ \mu\text{m}$ below the split surface, the IPF map shows the formation of very small, equiaxed (sub-)grains in the vicinity of the indents with orientations deviating from the rolling-type texture. These grains as well as an increase in the local orientation spread are only found in a radius of $\approx 1\ \mu\text{m}$ around the indents. However, the pile-up region spans 2–3 times this distance perpendicular to the elongation direction. Parallel to the grain elongation direction, there are only minor differences between the expansion of the pile-up and the orientation rotations. This leads to assumption that the plastic deformation is not only carried by dislocation activity, but also by a grain boundary-mediated

deformation mechanism that causes the formation of steps at the sample surface.

To investigate the possible grain boundary mediated deformation mechanisms, incremental pillar compression experiments were carried out. **Figure 4** (left) shows the initial microstructure of one of the faceted pillars. It exhibits the strongly elongated structure with rolling-type texture that is characteristic for the region close to the split surface as already shown in Figure 1. The pillar contains nearly 100 grains along its height but only very few grains in grain elongation direction as many grains span over the full width of the pillar.

The BSE images in Figure 4 show the deformation behavior of faceted pillars with increasing strain. During the first strain increments, the lower part of the pillar is nearly unaffected. This phenomenon can be attributed to the taper angle of the pillar caused by FIB milling that leads to an increase in cross-sectional area from top to bottom. For Pillar #1, the deformation in the upper part starts localized at grain boundaries, as shown by the appearance of the bright-dark contrast in the microstructure. This evolving contrast is due to the shift of

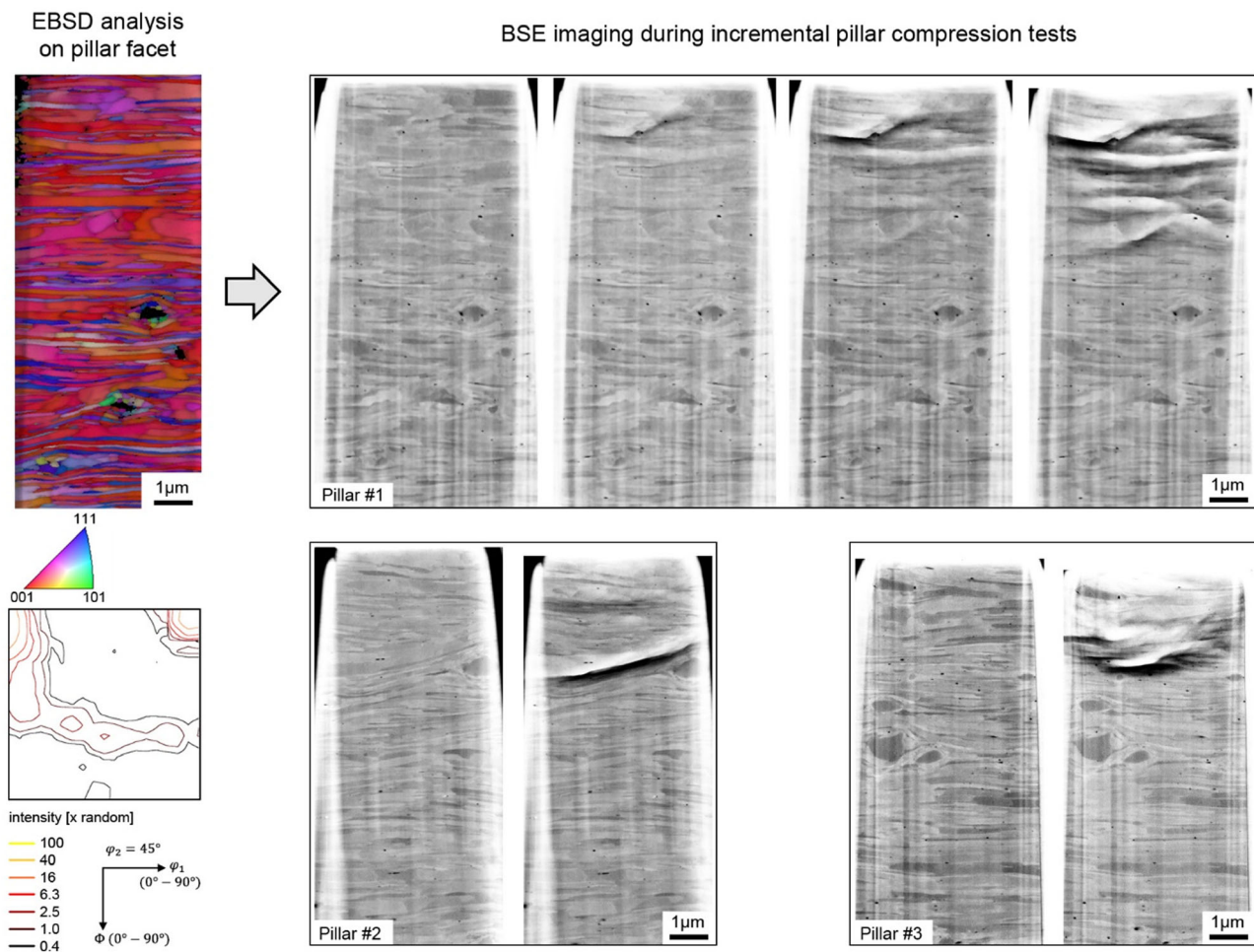


Figure 4. EBSD analysis on facet of Pillar #1 prior to compression testing (left) and BSE images from incremental pillar compression tests (right), showing the evolution with increasing strain (Pillar #1) and the initial and final stage for two other pillars (Pillar #2 and Pillar #3).

the brighter area toward the viewing direction. With increasing strain, the plastic deformation expands to lower regions, some of which show a more gradual change in surface roughness as would be expected in case of dislocation slip within individual grains. The ratio between highly localized plasticity creating discrete steps in the surface versus more homogeneous plasticity with less localized roughening varies between the different pillars but both features are found in all pillars that have been tested (Figure 4).

To determine possible correlations between microstructural characteristics and the sites of localizations, the microstructure of a moderately strained pillar (Pillar #1) is investigated before and after the deformation. The localizations occurring during the deformation of this pillar as shown in Figure 4 are marked in the IPF map, the Taylor factor map, as well as the grain boundary misorientation map of its initial microstructure in Figure 5.

This figure does not display any significant correlations between the local orientations or Taylor factors of grains and the occurrence of localizations between them. There are some localizations between grains with strongly differing Taylor factors, yet this is not the case for all localizations. Considering that frequent crystal orientations such as the rotated cube component and orientations along the gamma fiber exhibit strong differences in their Taylor factors, differing Taylor factors between neighboring grains are a relatively common feature. Since only very few of these boundaries show strain localizations, there is no indication that this phenomenon is related to strong gradients in the amount of plastic work during compressions that the Taylor factor represents. The grain boundary

misorientation in the areas of localizations does not exhibit a clear trend either. However, the misorientations based on EBSD analyses have to be treated with caution, since the BSE images suggest the existence of some very thin grains within the pillar that possibly lies beyond the resolution of the EBSD analysis.

The comparison of the microstructure of Pillar #1 before testing to the one found after compression and FIB polishing in Figure 6 does not show any substantial deviations near the strain localization sites. There is no observable change of local orientations that would be a sign of dislocation activity in these areas. Small changes in the grain geometry can be seen in the area of the topmost localizations where very small grains are found. The area of other localizations though does not exhibit changes in geometry. Therefore, it is more likely that this observed change in grain size is due to pre-existing deviations in grain geometry in transverse direction.

The faceted geometry of the pillars and incremental loading and unloading procedure for intermediate imaging complicate the determination of stress–strain curves. Therefore, cylindrical pillars with 5 μm and 10 μm diameter were tested as a reference to assess the flow stress as well as the strain rate sensitivity. The exemplary stress–strain curves in Figure A1 show that pillars with both diameters yield at ≈ 1200 MPa. In all experiments, the SRJs triggered unstable deformation (horizontal sections), which prevents a reliable quantification of the strain rate sensitivity. A rough estimate based on the change in flow stress with increasing strain rate (e.g., second SRJ of 10 μm pillar in Figure 7) provides an m -value of ≈ 0.02 , which is in line with the indentation experiments.

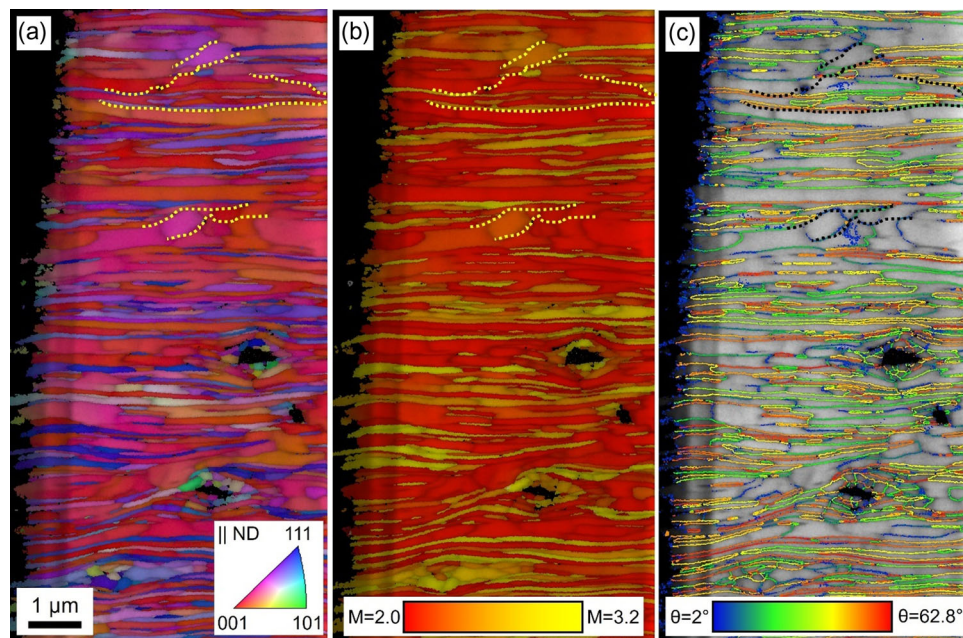


Figure 5. EBSD analysis of Pillar #1 prior to compression testing showing image quality maps with a) superimposed IPF map, b) Taylor factor map for uniaxial compression, and c) grain boundary misorientations. Deformation localization sites that were later observed during testing are marked with dotted lines.

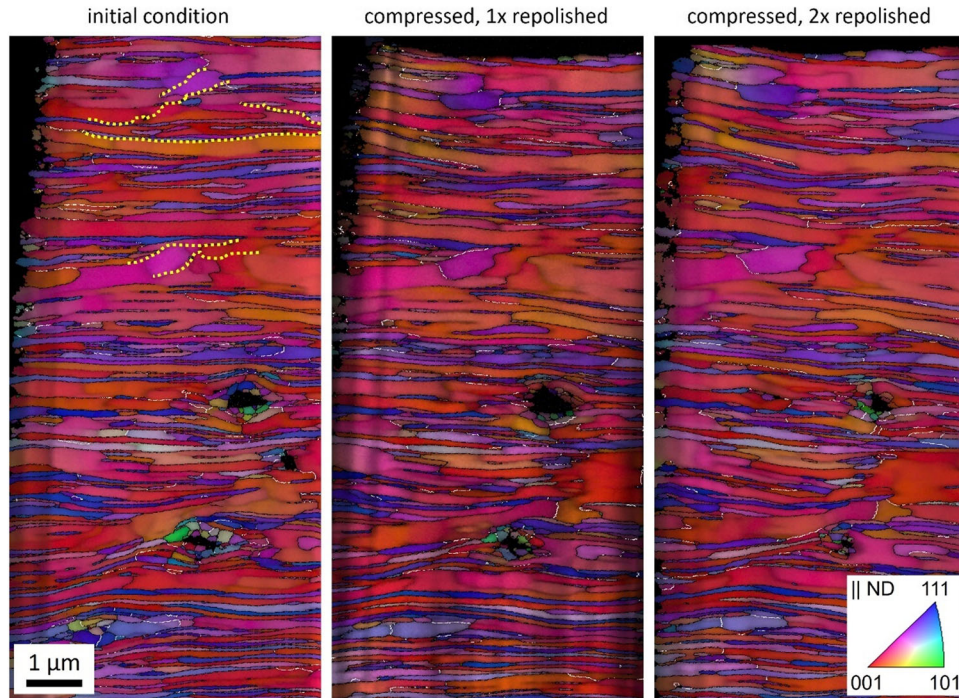


Figure 6. IPF maps of Pillar #1: initial microstructure prior to compression testing (left) and after deformation and repolishing (middle) and after removal of additional 200 nm from the facet (right). Localization sites of the deformation during compression testing are marked yellow in the initial condition.

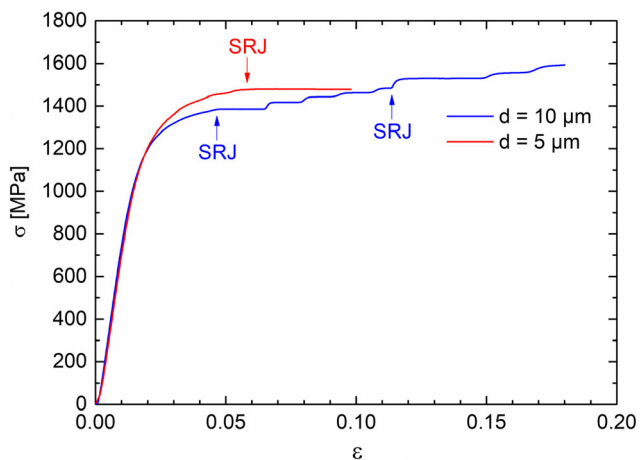


Figure 7. Engineering stress–strain curves from pillar compression tests with SRJ. The initial displacement rate was set to 10 nm s^{-1} and reduced to 1 nm s^{-1} at the first SRJ and increased to 10 nm s^{-1} in case of the $10 \text{ }\mu\text{m}$ -diameter pillar at a second SRJ.

4. Discussion

4.1. Deformation Mechanisms

The pillar experiments showed that the deformation of the pillar is carried almost exclusively by the translation of grains against

each other along their shared grain boundary. This observation is astonishing considering the unfavorable orientation of nearly 90° to the loading axis of most grain boundaries in the pillars, which suggests that little-to-no shear stress acts in their plane. A small shear stress can be assumed for the grain boundary segments that deviate from this angle. Due to geometric reasons, this has to be the case at all triple junctions, implying that some amount of shear stress has to act on every grain boundary segment between triple junctions. However, this stress will be low compared to the applied stress, which is why the underlying mechanism seems to operate at low shear stresses within the boundaries. The local initial stress state within the grain boundaries that results from the processing is unknown and might contribute to the observed phenomenon; yet, its impact is limited by the pillar geometry and stress relaxation caused by the lack of lateral constraints.

The observations made in the pillar experiments will be used to identify the underlying mechanism that carries the grain boundary-mediated deformation. As discussed in the Introduction, several mechanisms are reported for UFG and NC materials. Their possible role in the LFS-produced UFG microstructure will be addressed in the following paragraphs.

Shear band formation as well as grain rotation can be ruled out as a dominant deformation mechanism in the present material by comparing the initial microstructure to the one after deformation. The highly elongated grain shape also geometrically impedes grain rotations.

Grain boundary migration was discussed as the reason for the formation of a steady state in cold rolling following HPT,^[17] allowing further deformation without accompanying grain refinement. This suggests that this mechanism might also be dominant in the investigated LFS UFG microstructure, since the formation of a steady state is also observed during LFS.^[30,32,34] A coupled motion between grain boundary migration in its normal direction and in-plane translation^[35] is not likely to cause the observed relative motion. There is a coupling factor between both translations that always leads to a higher migration distance in normal direction as compared to the translation distance.^[36] This is disproved by the comparison of the microstructure before and after deformation that does not show significant changes in grain thickness at the localizations. Furthermore, a coupled motion should rather lead to an inclination of surface segments than the formation of discrete steps.

Another possible deformation mechanism is grain boundary sliding, which can either be diffusion based or being mediated by grain boundary dislocations. The strain rate achievable by diffusion-based grain boundary sliding (Coble creep) is strongly dependent on the grain size of the material. An upper estimate can be calculated using the smallest effective grain size occurring in an HC480LA LFS profile that is ≈ 200 nm.^[37] A stress of 1.5 GPa as an upper estimate from the pillar compression tests (Figure 7) would result in a Coble creep rate $\dot{\epsilon}_{\text{Coble}} \approx 1.5 \times 10^{-14} \text{ s}^{-1}$ ^[38] using the extrapolated grain boundary diffusion coefficient of iron at room temperature of $D_{\text{GB}} \approx 10^{-27} \frac{\text{m}^2}{\text{s}}$.^[39] This assumption might underestimate the creep rate given that for some NC materials grain boundary diffusion coefficients can be increased by up to four orders of magnitude.^[21,40] However, coble creep rates have a linear relation to the grain boundary diffusion coefficient; hence, they would have to increase by about ten orders of magnitude to approach the strain rates during pillar compression tests or indentation experiments and even more for the strain rates imposed during the LFS processing of the material.^[24,27] Consequently, diffusion-based grain boundary sliding cannot play a substantial role in the deformation behavior of this material. This is also confirmed by the strain rate sensitivity $m \approx 0.02$, which should approach $m \approx 1$ ^[41] in case of diffusion-based grain boundary sliding.

Based on the principle of exclusion, the motion of grain boundary dislocations as carrier for the observed localized deformation appears to be the most likely case. In this scenario, the plasticity would be mainly affected by triple junctions at which grain boundary dislocations pile up. However, due to the elongated grain shape, this resistance is supposedly low for two reasons. First, the average spacing between triple junctions in sliding direction of $\approx 1\text{--}2 \mu\text{m}$ is relatively high. In case of pillar compression with a diameter of $5 \mu\text{m}$, there may even be not a single triple junction present between some pairs of neighboring grains. Second, the triple junction angles at the tips of elongated grains strongly deviate from the equilibrium value of 120° .^[31] In contrast to equilibrium triple junctions, smaller triple junction angles were found to exhibit a much lower resistance to grain boundary dislocation motion by Fedorov et al.^[42,43] Hence, the microstructural topology should

favor grain boundary dislocation-based plasticity, which is potentially further enhanced in unconstrained small volumes such as micropillars.

Looking at the angles between the loading axis in pillar compression tests and the observed direction of grain boundary sliding, the shear stresses acting in the plane of relative motion can be estimated. The actual angles aren't fully assessable in all cases, but it appears that they are often very high, reaching values around 80° . In that case, the shear stress acting in the boundary will be less than 20% of the principle stress in loading direction. Considering the observed stress levels from pillar compression tests (Figure 7), it appears that grain boundary sliding can already occur at interfacial shear stresses of 300 MPa or even lower.

4.2. Implications for Bulk Behavior

Due to the small material volume in the tested pillars, the question remains whether the observation of localized deformation is purely due to geometric reasons or is also transferable to the bulk material. Since the pillar diameter is only slightly higher than the grain diameter in this direction, nearly no accommodation processes are necessary to allow grain boundary sliding. This should decrease the stress required for the initiation of the grain boundary sliding process. However, the flow stress of the pillars at plastic strains comparable to nanoindentation tests of ≈ 1400 MPa does not indicate a pronounced softening of the material due to the lack of lateral constraints. Based on the indentation hardness for $\dot{\epsilon} = 10^{-3} \text{ s}^{-1}$ (Figure 2), one would expect a flow stress of ≈ 1550 MPa (assuming a constraint factor of 3), which is only 10% higher than the measured value. Hence, the grain boundary sliding mechanism in the pillars is most likely enhanced by the lack of lateral constraints but the localization phenomenon is unlikely to be just caused by the geometry while being entirely absent in more constraint loading scenarios.

The formation of steps along grain boundaries on the sample surface around the indents in $30 \mu\text{m}$ distance to the surface outside the zone of dislocation activity can also be attributed to grain boundary sliding. Therefore, the observations in the pillars can be transferred to the "semibulk" behavior of the material around indents. Even though the formation of surface steps is used as an indication for grain boundary sliding in several studies,^[8,16,22] some authors argue that the sliding is confined to the very surface due to the lacking constraint at the free surface.^[44] While this may be a valid point for equiaxed grains, the situation is different for the lamellar microstructure in the present work where the grain size perpendicular to the sample surface is in the order of several microns. Therefore, the grains exhibiting grain boundary sliding processes span a distance to the surface in the same order of magnitude as the plastic zone size below the indent that can be estimated using Tabor's approach to be $\approx 3 \mu\text{m}$.^[45,46] Consequently, the grain boundary sliding has to occur in a significant part of the plastic zone. To which extent this process also occurs within the bulk of LFS profiles, or UFG microstructures generated by SPD processes in general, cannot be answered at this stage. Geometric constraints and necessary

accommodation processes will affect the deformation behavior in bulk material, which should either reduce the contribution of grain boundary sliding in the presence of competing processes operating at a similar flow stress or increase the flow stress accordingly. While the elongated microstructure in LFS profiles facilitates the observation of the sliding process, this does not imply that it can only occur in similar microstructures. In the present case, the shear stresses acting in the boundary are relatively small compared to the principal stresses as the inclination angle of the boundaries showing the sliding phenomenon is far from 45° to the loading axis. In an equiaxed microstructure, a considerable fraction of the total grain boundary area would be exposed to higher shear stresses than the ones required to trigger the sliding processes in the pillar compression test, which could counteract the effect of lateral constraints.

An obvious approach to check if the mechanism also occurs in the bulk of LFS processes would be to look at the crystallographic texture. It can be considered as a fingerprint of the active deformation mechanisms and has been used to derive slip of dislocation partials as well as grain boundary sliding in NC materials.^[11,12] However, this approach is not straightforward in the present case. The strong bcc rolling texture observed in the lamellar UFG microstructure does indicate that the deformation mode during grain refinement is predominantly dislocation slip under plane strain compression but qualitatively, it cannot disprove or confirm a grain boundary sliding processes. Grain boundary sliding in a lamellar microstructure as observed in pillar compression tests would mostly conserve the pre-existing texture, thus leaving little-to-no footprint.

5. Summary and Conclusions

The deformation behavior of a ferritic steel with a UFG lamellar microstructure has been studied around indents as well as in

pillar compression tests using a faceted geometry to facilitate microstructural investigations. The key results are summarized as follows.

- The pile-up behavior around indents in the UFG lamellar microstructure shows a pronounced anisotropy with protrusions parallel to the elongation direction related to blocks of lamellar grains being shifted against each other.
- Micropillar compression tests with complementary microstructural analyses reveal two deformation modes:
 - 1) sliding of lamellar grains against creating sharp edges at the surface.
 - 2) intragranular dislocation slip leading to a more gradual surface roughening.
- The flow stress in pillar compression experiments is $\approx 10\%$ lower than the expected value based on nanoindentation hardness data. This indicates that there may be some geometric softening in the pillar due to the lack of lateral constraints but not to the point that entirely different deformation mechanisms are expected.
- The grain boundary sliding process is only observed for some boundaries with no apparent correlation in terms of misorientation angle, inclination to the loading axis, or gradient in the Taylor factor of the neighboring grains.
- The strain rate sensitivity m in nanoindentation and pillar compression is ≈ 0.02 , which is in line with literature data for bcc Fe with UFG microstructure and indicates dislocation-based plasticity.
- Based on the sum of observations, the grain boundary sliding processes observed in nanoindentation and pillar compression experiments is assumed to be carried by grain boundary dislocations.

Appendix

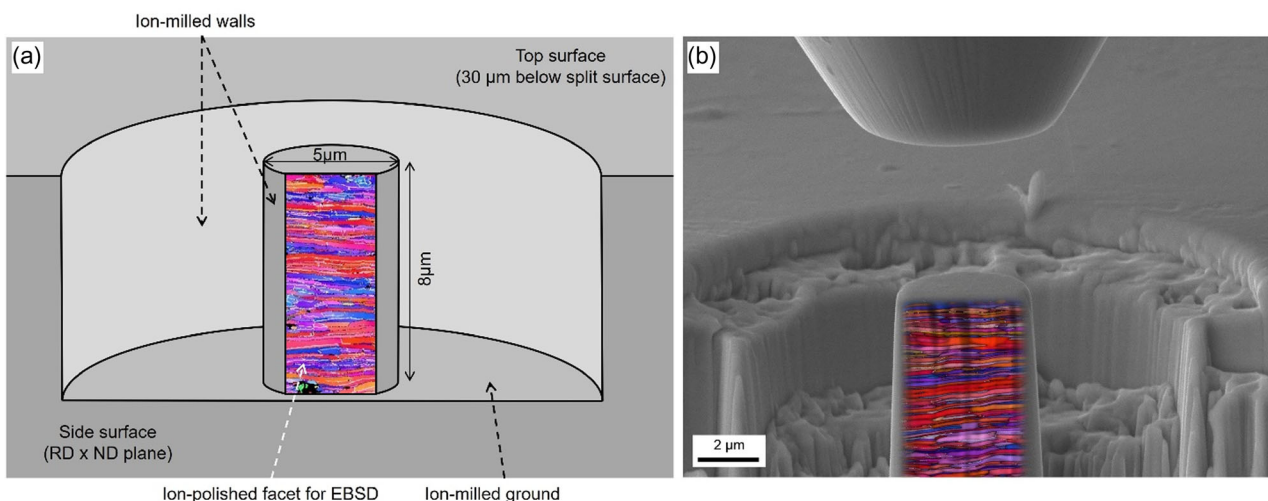


Figure A1. a) Schematic image of faceted micropillars used in this work and b) SE image of a pillar and flat punch indenter showing the IPF map of the ion-polished pillar facet as overlay.

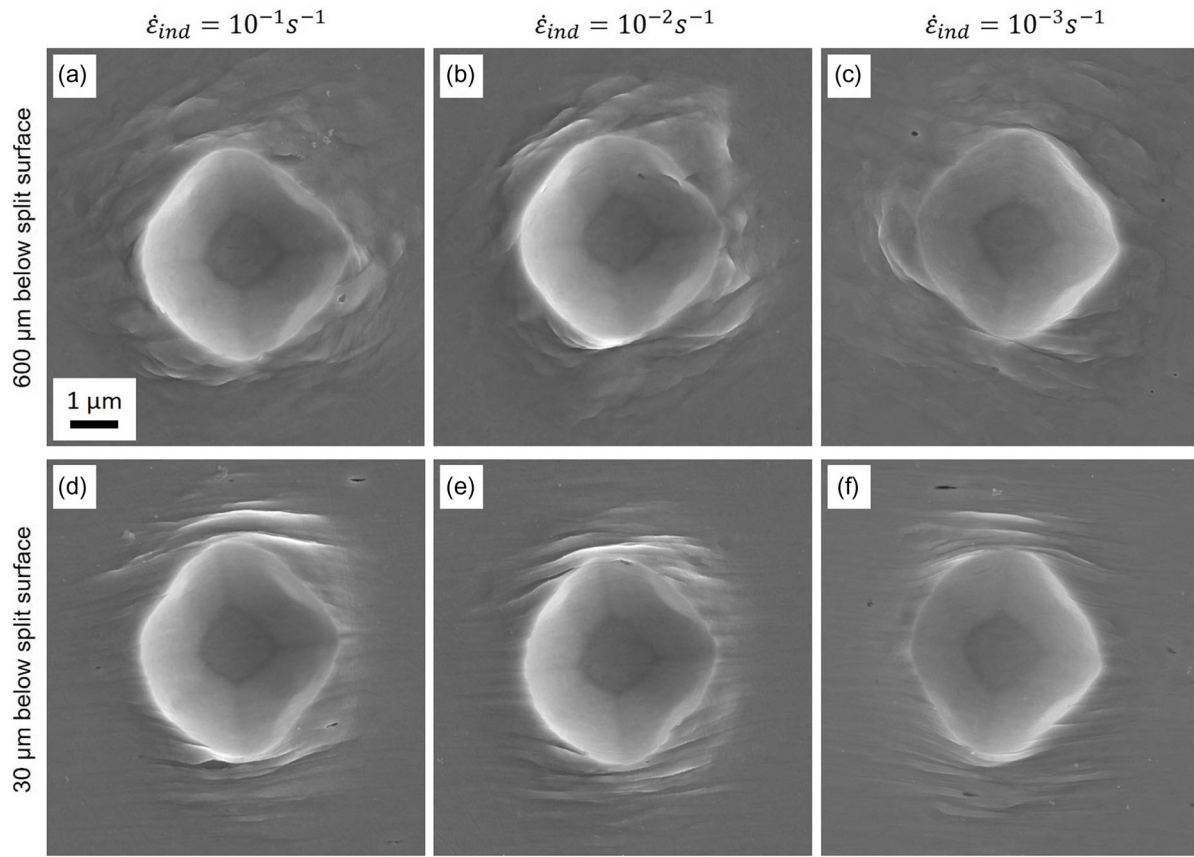


Figure A2. SE images showing deformation characteristic on the surface (RD × ND plane) around indents in a–c) 600 μm and d–f) 30 μm distance to the split surface at different strain rates: a,d) $\dot{\epsilon}_{ind} = 10^{-1} s^{-1}$, b,e) $\dot{\epsilon}_{ind} = 10^{-2} s^{-1}$, and c,f) $\dot{\epsilon}_{ind} = 10^{-3} s^{-1}$.

Acknowledgements

Parts of this work were performed with the support of the Karlsruhe Nano Micro Facility (KNMF, www.knmf.kit.edu), a Helmholtz Research Infrastructure at Karlsruhe Institute of Technology (KIT). The authors greatly appreciate the focused ion beam preparation and valuable inputs by Torsten Scherer (KIT). Parts of this work were carried out within the framework of the Collaborative Research Center 666 (subproject C1), funded by the German Research Foundation (DFG).

Open Access funding enabled and organized by Projekt DEAL.

Received: February 1, 2024

Revised: May 8, 2024

Published online: May 25, 2024

Conflict of Interest

The authors declare no conflict of interest.

Data Availability Statement

The data that support the findings of this study are available from the corresponding author upon reasonable request.

Keywords

grain boundary sliding, nanoindentations, pillar compressions, ultrafine-grained microstructures

- [1] H. Conrad, *Mater. Sci. Eng. A* **2003**, *341*, 216.
- [2] K. A. Padmanabhan, G. P. Dinda, H. Hahn, H. Gleiter, *Mater. Sci. Eng. A* **2007**, *452–453*, 462.
- [3] N. Tsuji, Y. Ito, Y. Saito, Y. Minamino, *Scr. Mater.* **2002**, *47*, 893.
- [4] Y. M. Wang, E. Ma, M. W. Chen, *Appl. Phys. Lett.* **2002**, *80*, 2395.
- [5] M. A. Meyers, A. Mishra, D. J. Benson, *Prog. Mater. Sci.* **2006**, *51*, 427.
- [6] H. Conrad, *Nanotechnology* **2007**, *18*, 325701.
- [7] R. Pippin, S. Scheriau, A. Taylor, M. Hafok, A. Hohenwarter, A. Bachmaier, *Annu. Rev. Mater. Res.* **2010**, *40*, 319.
- [8] N. Q. Chinh, P. Szommer, Z. Horita, T. G. Langdon, *Adv. Mater.* **2006**, *18*, 34.
- [9] T. Matsunaga, S. Itoh, Y. Satoh, H. Abe, *Mater. Sci. Eng. A* **2013**, *576*, 267.
- [10] I. Sabirov, Y. Estrin, M. R. Barnett, I. Timokhina, P. D. Hodgson, *Acta Mater.* **2008**, *56*, 2223.
- [11] L. S. Toth, W. Skrotzki, Y. Zhao, A. Pukenas, C. Braun, R. Birringer, *Materials* **2018**, *11*, 190.
- [12] W. Skrotzki, A. Eschke, B. Jóni, T. Ungár, L. S. Tóth, Y. Ivanisenko, L. Kurmanaeva, *Acta Mater.* **2013**, *61*, 7271.
- [13] M. J. Zehetbauer, Y. T. Zhu, in *Bulk Nanostructured Materials*, Wiley-VCH Verlag GmbH & Co. KGaA, Weinheim **2009**.

- [14] D. Jia, K. T. Ramesh, E. Ma, *Acta Mater.* **2003**, *51*, 3495.
- [15] Q. Wei, D. Jia, K. T. Ramesh, E. Ma, *Appl. Phys. Lett.* **2002**, *81*, 1240.
- [16] A. Vinogradov, S. Hashimoto, V. Patlan, K. Kitagawa, *Mater. Sci. Eng. A* **2001**, *319–321*, 862.
- [17] O. Renk, A. Hohenwarter, S. Wurster, R. Pippan, *Acta Mater.* **2014**, *77*, 401.
- [18] A. V. Sergueeva, N. A. Mara, A. K. Mukherjee, *J. Mater. Sci.* **2007**, *42*, 1433.
- [19] M. Y. Gutkin, I. A. Ovid'ko, C. S. Pande, *Philos. Mag.* **2004**, *84*, 847.
- [20] R. A. Masumura, P. M. Hazzledine, C. S. Pande, *Acta Mater.* **1998**, *46*, 4527.
- [21] H. S. Kim, Y. Estrin, M. B. Bush, *Acta Mater.* **2000**, *48*, 493.
- [22] K. V. Ivanov, E. V. Naydenkin, *Scr. Mater.* **2012**, *66*, 511.
- [23] M. Hafok, R. Pippan, *Scr. Mater.* **2007**, *56*, 757.
- [24] C. Müller, T. Bohn, E. Bruder, T. Bruder, V. Landersheim, C. el Dsoki, P. Groche, et al., *Materialwiss. Werkstofftech.* **2007**, *38*, 842.
- [25] C. Müller, T. Bohn, E. Bruder, P. Groche, *Mater. Sci. Forum* **2008**, *584–586*, 68.
- [26] L. Ahmels, D. Dehtyriov, E. Bruder, A. Molotnikov, *Adv. Eng. Mater.* **2021**, *23*.
- [27] P. Groche, D. Vucic, M. Jöckel, *J. Mater. Process. Technol.* **2007**, *183*, 249.
- [28] *Manufacturing Integrated Design: Sheet Metal Product and Process Innovation* (Eds: P. Groche, E. Bruder, S. Gramlich), Springer, Cham **2017**.
- [29] E. Bruder, T. Bohn, C. Müller, *Mater. Sci. Forum* **2008**, *584–586*, 661.
- [30] L. Ahmels, A.-K. Bott, E. Bruder, M. Gibbels, S. Gramlich, M. Hansmann, I. Karin, et al., in *Manufacturing Integrated Design: Sheet Metal Product and Process Innovation* (Eds: P. Groche, E. Bruder, S. Gramlich), Springer, Cham **2017**.
- [31] L. Ahmels, A. Kashiwar, T. Scherer, C. Kübel, E. Bruder, *J. Mater. Sci.* **2019**, *54*, 10489.
- [32] T. Bohn, E. Bruder, C. Müller, *J. Mater. Sci.* **2008**, *43*, 7307.
- [33] Q. Wei, S. Cheng, K. T. Ramesh, E. Ma, *Mater. Sci. Eng. A* **2004**, *381*, 71.
- [34] E. Bruder, L. Ahmels, J. Niehuesbernd, C. Müller, *Materialwiss. Werkstofftech.* **2017**, *48*, 41.
- [35] J. W. Cahn, J. E. Taylor, *Acta Mater.* **2004**, *52*, 4887.
- [36] L.-L. Niu, X. Shu, Y. Zhang, F. Gao, S. Jin, H.-B. Zhou, G.-H. Lu, *Mater. Sci. Eng. A* **2016**, *677*, 20.
- [37] J. Niehuesbernd, E. Bruder, C. Müller, *Mater. Sci. Eng. A* **2018**, *711*, 325.
- [38] R. L. Coble, *J. Appl. Phys.* **1963**, *34*, 1679.
- [39] A. Inoue, H. Nitta, Y. Iijima, *Acta Mater.* **2007**, *55*, 5910.
- [40] J. Horváth, R. Birringer, H. Gleiter, *Solid State Commun.* **1987**, *62*, 319.
- [41] Y. Wang, A. Hamza, E. Ma, *Acta Mater.* **2006**, *54*, 2715.
- [42] A. A. Fedorov, M. Y. Gutkin, I. A. Ovid'ko, *Acta Mater.* **2003**, *51*, 887.
- [43] R. Hull, R. M. Osgood, J. Parisi, H. Warlimont, M. Y. Gutkin, I. A. Ovid'ko, in *Plastic Deformation in Nanocrystalline Materials*, Springer, Berlin, Heidelberg **2004**.
- [44] A. Böhner, V. Maier, K. Durst, H. W. Höppel, M. Göken, *Adv. Eng. Mater.* **2011**, *13*, 251.
- [45] D. Kramer, H. Huang, M. Kriese, J. Robach, J. Nelson, A. Wright, D. Bahr, et al., *Acta Mater.* **1998**, *47*, 333.
- [46] W. Zielinski, H. Huang, W. W. Gerberich, *J. Mater. Res.* **1993**, *8*, 1300.